# Asymmetrical in-fiber Mach-Zehnder interferometer for curvature measurement

**Bing Sun, Yijian Huang, Shen Liu, Chao Wang, Jun He, Changrui Liao, Guolu Yin, Jing Zhao, Yinjie Liu, Jian Tang, Jiangtao Zhou, and Yiping Wang[*]**

*Key Laboratory of Optoelectronic Devices and Systems of Ministry of Education and Guangdong Province, College of Optoelectronic Engineering, Shenzhen University, Shenzhen 518060, China*
[*]*ypwang@szu.edu.cn*

**Abstract:** We demonstrated a compact and highly-sensitive curvature sensor based on a Mach-Zehnder interferometer created in a photonic crystal fiber. Such a Mach-Zehnder interferometer consisted of a peanut-like section and an abrupt taper achieved by use of an optimized electrical arc discharge technique, where only one dominating cladding mode was excited and interfered with the fundamental mode. The unique structure exhibited a high curvature sensitivity of 50.5 nm/m$^{-1}$ within a range from 0 to 2.8 m$^{-1}$, which made it suitable for high-sensitivity curvature sensing in harsh environments. Moreover, it also exhibited a temperature sensitivity of 11.7 pm/°C.

## References and links

1. C. C. Ye, S. W. James, and R. P. Tatam, "Simultaneous temperature and bend sensing with long-period fiber gratings," Opt. Lett. **25**(14), 1007–1009 (2000).
2. Y.-G. Han, X. Dong, J. H. Lee, and S. B. Lee, "Simultaneous measurement of bending and temperature based on a single sampled chirped fiber Bragg grating embedded on a flexible cantilever beam," Opt. Lett. **31**(19), 2839–2841 (2006).
3. O. Frazão, J. Viegas, P. Caldas, J. L. Santos, F. M. Araújo, L. A. Ferreira, and F. Farahi, "All-fiber Mach-Zehnder curvature sensor based on multimode interference combined with a long-period grating," Opt. Lett. **32**(21), 3074–3076 (2007).
4. Y.-G. Han, G. Kim, K. Lee, S. B. Lee, C. H. Jeong, C. H. Oh, and H. J. Kang, "Bending sensitivity of long-period fiber gratings inscribed in holey fibers depending on an axial rotation angle," Opt. Express **15**(20), 12866–12871 (2007).
5. P. Saffari, T. Allsop, A. Adebayo, D. Webb, R. Haynes, and M. M. Roth, "Long period grating in multicore optical fiber: an ultra-sensitive vector bending sensor for low curvatures," Opt. Lett. **39**(12), 3508–3511 (2014).
6. Y. P. Wang and Y. J. Rao, "A novel long period fiber grating sensor measuring curvature and determining bend-direction simultaneously," IEEE Sens. J. **5**(5), 839–843 (2005).
7. L. Wang, W. Zhang, P. Geng, S. Gao, J. Li, Z. Bai, L. Chen, S. Zhang, Y. Liu, and T. Yan, "Simultaneous directional bending and temperature measurement with overlapping long period grating and fiber Bragg grating structure," J. Opt. **16**(5), 055401 (2014).
8. Z. Wu, Y.-G. Liu, Z. Wang, M. Jiang, W. Ji, T. Han, S. Li, X. Shao, X. Q. Dinh, S. C. Tjin, and P. P. Shum, "Simultaneous measurement of curvature and strain based on fiber Bragg grating in two-dimensional waveguide array fiber," Opt. Lett. **38**(20), 4070–4073 (2013).
9. C. Gouveia, P. A. S. Jorge, J. M. Baptista, and O. Frazao, "Temperature-independent curvature sensor using FBG cladding modes based on a core misaligned splice," IEEE Photon. Technol. Lett. **23**(12), 804–806 (2011).
10. Y. Gong, T. Zhao, Y.-J. Rao, and Y. Wu, "All-fiber curvature sensor based on multimode interference," IEEE Photon. Technol. Lett. **23**(11), 679–681 (2011).
11. R. Wang, J. Zhang, Y. Weng, Q. Rong, Y. Ma, Z. Feng, M. Hu, and X. Qiao, "Highly Sensitive Curvature Sensor Using an In-Fiber Mach-Zehnder Interferometer," IEEE Sens. J. **13**(5), 1766–1770 (2013).
12. C. Shen, C. Zhong, Y. You, J. Chu, X. Zou, X. Dong, Y. Jin, J. Wang, and H. Gong, "Polarization-dependent curvature sensor based on an in-fiber Mach-Zehnder interferometer with a difference arithmetic demodulation method," Opt. Express **20**(14), 15406–15417 (2012).
13. Y. Lu, C. Shen, C. Zhong, D. Chen, X. Dong, and J. Cai, "Refractive index and temperature sensor based on double-pass M-Z interferometer with an FBG," IEEE Photon. Technol. Lett. **26**(11), 1124–1127 (2014).
14. Y. Qi, L. Ma, Z. Kang, Y. Bai, B. Yin, and S. Jian, "Highly sensitive curvature sensor based on a multicladding fiber sandwiched dual no-core fibers structure," Appl. Opt. **53**(28), 6382–6388 (2014).

15. Y. Zhang, A. Zhou, B. Qin, Q. Xu, Z. Liu, J. Yang, and L. Yuan, "Simultaneous Measurement of Temperature and Curvature Based on Hollow Annular Core Fiber," IEEE Photon. Technol. Lett. **26**(11), 1128–1131 (2014).
16. S. Zhang, W. Zhang, S. Gao, P. Geng, and X. Xue, "Fiber-optic bending vector sensor based on Mach-Zehnder interferometer exploiting lateral-offset and up-taper," Opt. Lett. **37**(21), 4480–4482 (2012).
17. J. R. Guzman-Sepulveda and D. A. May-Arrioja, "In-fiber directional coupler for high-sensitivity curvature measurement," Opt. Express **21**(10), 11853–11861 (2013).
18. D. Wu, T. Zhu, K. S. Chiang, and M. Deng, "All Single-Mode Fiber Mach-Zehnder Interferometer Based on Two Peanut-Shape Structures," J. Lightwave Technol. **30**(5), 805–810 (2012).
19. H. Gong, X. Yang, K. Ni, C.-L. Zhao, and X. Dong, "An Optical Fiber Curvature Sensor Based on Two Peanut-Shape Structures Modal Interferometer," IEEE Photon. Technol. Lett. **26**(1), 22–24 (2014).
20. H. Y. Choi, M. J. Kim, and B. H. Lee, "All-fiber Mach-Zehnder type interferometers formed in photonic crystal fiber," Opt. Express **15**(9), 5711–5720 (2007).
21. Z. Ou, Y. Yu, P. Yan, J. Wang, Q. Huang, X. Chen, C. Du, and H. Wei, "Ambient refractive index-independent bending vector sensor based on seven-core photonic crystal fiber using lateral offset splicing," Opt. Express **21**(20), 23812–23821 (2013).
22. H. Gong, H. Song, S. Zhang, Y. Jin, and X. Dong, "Curvature Sensor Based on Hollow-Core Photonic Crystal Fiber Sagnac Interferometer," IEEE Sens. J. **14**(3), 777–780 (2014).
23. S. Guan and Q. Yu, "Index-insensitive curvature sensor based on holey fiber modal interferometer," Microw. Opt. Technol. Lett. **56**(7), 1709–1711 (2014).
24. M. Deng, C.-P. Tang, T. Zhu, and Y.-J. Rao, "Highly sensitive bend sensor based on Mach–Zehnder interferometer using photonic crystal fiber," Opt. Commun. **284**(12), 2849–2853 (2011).
25. H. Gong, H. Song, X. Li, J. Wang, and X. Dong, "An optical fiber curvature sensor based on photonic crystal fiber modal interferometer," Sens. Actuat, A-Phys. **195**, 139–141 (2013).
26. K. Ni, T. Li, L. Hu, W. Qian, Q. Zhang, and S. Jin, "Temperature-independent curvature sensor based on tapered photonic crystal fiber interferometer," Opt. Commun. **285**(24), 5148–5150 (2012).
27. J. H. Lim, H. S. Jang, K. S. Lee, J. C. Kim, and B. H. Lee, "Mach-Zehnder interferometer formed in a photonic crystal fiber based on a pair of long-period fiber gratings," Opt. Lett. **29**(4), 346–348 (2004).

## 1. Introduction

A variety of fiber-based curvature sensors have arisen due to their various applications in the areas of aerospace, geophysics, mechanical engineering, robotic arms, and structural health monitoring etc. Several schemes of fiber-optic curvature sensors based on the fiber gratings [1–9], the single-mode-multimode-single-mode (SMS) fiber structures [10], and interferometric structures [11–16] have been demonstrated. For instance, Gong et al. [10] proposed a fiber-optic curvature sensor based on a SMS structure with the maximum sensitivities of wavelength-curvature ($-10.38$ nm/m$^{-1}$) and intensity-curvature ($-130.37$ dB/m$^{-1}$) relationships. Among these fiber-based curvature sensors, those using fiber gratings or SMS as the sensing element could operate in large ranges of curvature but exhibit low sensitivity. Although a high-sensitivity curvature measurement based on twin-core directional coupler was demonstrated [17], it required expensive material cost, and besides, the splicing a twin-core fiber with a single mode fiber was a challenge.

The curvature sensor structure based on a Mach-Zehnder interferometer (MZI) usually involves two fiber-optic mode-coupling sections, where the two sections work as a beam splitter and a beam combiner. For instance, a single-mode fiber MZI consisting of two peanut-shape structures was used to investigate its response to the temperature and strain [18]. Recently, a curvature sensor has been reported, and it also consists of two peanut-shape sections [19]. In specially, MZIs formed in photonic crystal fibers (PCFs) have arisen due to their well-known superior advantages, such as east fabrication, compactness, and low temperature sensitivity. To make interference the fundamental mode with cladding modes, Choi et al. [20] proposed two methods, one is fusion splicing a PCF with a small lateral offset at a point and the other is partially collapsing the air holes of a single piece of PCF at a limited region. So far, a variety of curvature sensors by the means of exploiting PCFs have been investigated [21–27]. For example, Deng et al., demonstrated a sensitive curvature sensor, which consisted of a collapsed region and a small intentional lateral offsets [24]. However, either splicing with a lateral offset or collapsing a length of PCF would allow for more than two cladding modes interfering with the fundamental mode. And thus it would lead to a low extinction ratio or a small free spectral range, which is not suitable in the sensing field.

In this letter, we demonstrated a highly sensitive curvature sensor, which is based on an asymmetrical fiber MZI consisted of a peanut-like section and an abrupt taper. Such a unique structure exhibits a high sensitivity of 50.5 nm/m$^{-1}$, which is four times larger than the reported results in [16]. Moreover, the temperature cross-sensitivity can be lowered due to a small thermal-optic coefficient of the PCF.

## 2. Principle and experimental results

We employ a large mode area PCF (ESM-12, http://www.nktphotonics.com) and a single mode fiber (SMF-28) in our experiment, the SEM image of which is shown in Fig. 1(a). The structure of the proposed MZI, i.e. MZI-1, is shown in Fig. 1(c). Firstly, the propagating core mode guided in SMF-28 converts its partial power into a single cladding mode in the peanut-like section. As a result, the input optical signal is split into two optical path beams. And then the cladding mode is allowed to continue propagating through the holey structure of the PCF. Finally, an abrupt taper works as the beam combiner.
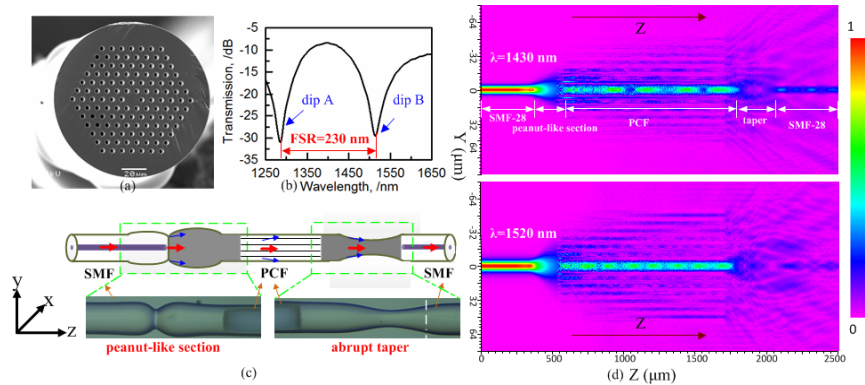


Fig. 1. (a) SEM image of the empoyed PCF. (b) Transmission spectrum of the fabricated MZI-1 (Sample 3). (c) Schematic diagram of the MZI-1 and microscopic images of the peanut-like section and abrupt taper shown in the left and right insets. (d) Beam propagation simulation in the MZI-1 at the wavelength of 1430 nm and 1520 nm, respectively.

A commercial fusion splicer (Fujikura FSM-80s) is employed. The parameters "Gapset Position" and "Overlap" in the fundamental program, i.e. "SM-SM" should be altered to fabricate the peanut-shaped section. Moreover, manual pushing both the sides of the PCF and the SMF-28 to the middle is required. The optimized splicing parameters are listed in Table 1. As shown in the left inset of Fig. 1(c), the peanut-like section is formed, where the diameters of the expanded section are ~180 and ~145 µm, respectively. Located a few millimeters away, an abrupt taper is carried out manually with the splicer (see the right inset in Fig. 1(c)). Here the corresponding splicing parameters are similar to that shown in Table 1 except that the "Taper splice" is used. As a result, we can see from Fig. 1(b) that strong interference spectrum can be observed and the insertion loss is less than 10 dB. In addition, a full-vectorial beam propagation simulation results with different wavelength are shown in Fig. 1(d), where the beam propagation direction is z-axis. It is indicated that the peanut-like section is beneficial to the power transformation between the fundamental mode and cladding modes in PCF, which induces strong mode interferences between them. Then the mode coupling continues to exist in the holey structure of the PCF until the abrupt taper region. As shown in Fig. 1(d), the power reaches the maximum point at the wavelength of 1430 nm, while it reaches the minimum point at the wavelength of 1520 nm.

**Table 1. Optimized splicing parameters for a commercial fusion splicer (Fujikura-80s)**

| Parameters | Units | Values |
|---|---|---|
| prefusion power | bit | standard |
| Prefusion time | ms | 180 |
| overlap | μm | 0 |
| fusion power | bit | Standard + 10 |
| Fusion time | ms | 1200 |
| offset | μm | −30 |

Firstly, the light propagating in SMF-28 is divided into two beams in the peanut-like section, one is the fundamental mode while the other one is the dominating cladding mode. Therefore, the proposed structure can be operated according to a dual-mode MZI. With the phase difference Φ between the core mode and the cladding mode, the interference will take place and the intensity of the output can be expressed as

$$\Phi = \frac{2\pi(n_{core,eff} - n_{clad,eff})L}{\lambda} \qquad (1)$$

$$I = I_{core} + I_{clad} + 2\sqrt{I_{core}I_{clad}}\cos\Phi \qquad (2)$$

where $n_{core,eff}$ and $n_{clad,eff}$ are the effective refractive indices of the core and cladding mode, respectively, L is the effective length of the MZI-1, $I_{core}$ and $I_{clad}$ are the intensities of the core mode and cladding mode, respectively. When $\Phi = (2m + 1)\pi$, m = 0, 1, 2..., the minimum wavelength value of the output light intensity is located at

$$\Phi = \frac{2\pi(n_{core,eff} - n_{clad,eff})L}{\lambda} \qquad (3)$$

$\Delta n_{eff}$ is the effective refractive index difference between $n_{core,eff}$ and $n_{clad,eff}$. As a result, the free spectral range (FSR) of such fiber interferometer can be expressed as

$$FSR = \frac{\lambda^2}{\Delta n_{eff}L} \qquad (4)$$

We have fabricated three samples in order to determine the number and power distribution of the modes involved in the interference pattern. And the spectra of three MZIs are Fast Fourier transformed to obtain the spatial frequency spectrums. As shown in Fig. 2(a), three modes including the fundamental mode and two cladding modes construct the interference pattern. Obviously, the power is primarily distributed in the fundamental mode and one of the cladding modes, while the other cladding mode has very small contribution to the interference pattern. Furthermore, the mode fields and refractive indices of the $LP_{01}$ ( $HE_{11}^{x}$ and $HE_{11}^{y}$ ) modes and the $LP_{11}$ ( $HE_{21}^{x}$, $HE_{21}^{y}$, $TE_{01}$ and $TM_{01}$ ) modes existed in the PCF are calculated by using the full-vectorial finite element method, as shown in Fig. 2(b). We can get value of $\Delta n_{eff}$ between the $LP_{01}$ mode and the $LP_{11}$ mode is ~2.989 × 10$^{-3}$ at λ = 1513 nm. According to Eq. (4), the corresponding FSR is calculated as 232.3 nm, which is close to the experimentally measured value in Fig. 1(c).
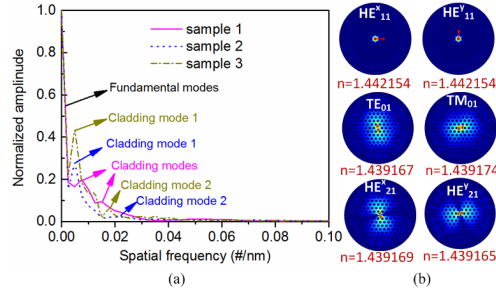
Fig. 2. (a) Spatial frequency spectra of the three samples. (b) The mode fields and refractive indices of the fundamental modes and cladding modes existed in sample 3 at the wavelength of 1513 nm.

The MZI-1 with 2.8 mm length (sample 3) was used to investigate its transmission spectra at different curvature with a supercontinuum white-light source (NKT SuperK Compact) and an optical spectrum analyzer (YOKOGAWA AQ6370C). The sensing section was fixed between two fiber holders among which a fiber holder could be moved longitudinally. The bent fiber was normally approximated as an arc of circle. So the sensor's curvature was given by

$$C = 1/R = 2d/(d^2 + L^2) \tag{5}$$

R is the curvature radius, d is the bending displacement, and L is the half distance between the edges of the two clamps, which is set as 104 mm.

The measured transmission spectra shift of the MZI-1 under different curvatures was shown in Fig. 3(a). It could be seen that the interference fringe shifts toward a longer wavelength, i.e. "red" shift with increasing curvature. The relationship between curvature and wavelength of dip A in the spectrum was plotted in Fig. 3(b). A linear response is obtained with a high sensitivity of 50.5 nm/m$^{-1}$. The intensity of the dip also has a litter change with the bending of the sensing section, as shown in Fig. 3(b). And we attribute it to different power ratios between the dominating fundamental mode and the cladding mode in the process of curvature measurement.
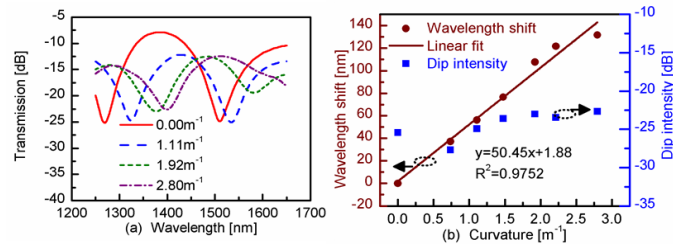


Fig. 3. (a) Spectra responces of the MZI-1 (sample 3) for different curvature. (b) The wavelength shift and dip intensity of the MZI-1 at dip A.

Temperature response of the MZI-1 was also investigated by means of placing it into a column oven with a temperature range from room temperature to 95 °C. In addition, a differential thermocouple (UNI-T UT320) was used to measure the temperature with an accuracy of 0.1 °C. It should be noted that the temperature in the oven rose gradually from 25 to 95 °C with a step of 10 °C, and then maintained about 20 min during each temperature rise. The wavelength shift induced by temperature was about 840 pm from 25 to 95 °C, i.e. a sensitivity of 11.7 pm/°C. In addition, there was nearly no variation in dip intensity been measured (Fig. 4).
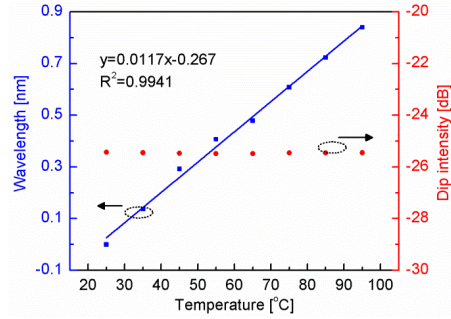
Fig. 4. The wavelength shift and dip intensity of the MZI-1 versus temperature at dip A.

Furthermore, the existence of the pair of asymmetrical sections, i.e. a peanut-like element and an abrupt taper, played a dominated role in the high curvature sensitivity. By comparison, we fabricated another PCF-based MZI without a peanut-like section and an abrupt taper, i.e. MZI-2, which consisted of two collapsed regions in the spliced joints. To serve as a contrast, the same physical length (~2.8 mm) is involved except for substituting the asymmetrical elements for the two collapsed regions. And the lengths of the two collapsed regions are ~142 and ~148 μm, respectively. It's obvious that the corresponding transmission spectra are irregular compared with the MZI-1, as shown in Fig. 5. And we conclude a comparative result with that reported in the references [23–26], where the curvature sensitivity (6.1 nm/m$^{-1}$) is an order lower than the result in the manuscript (50.5 nm/m$^{-1}$).
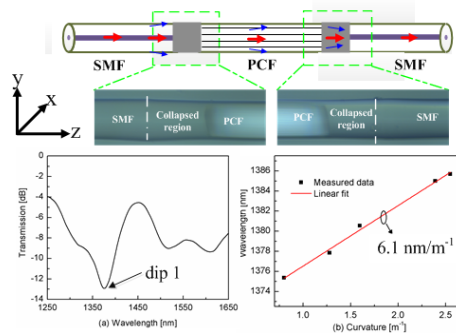


Fig. 5. (a) Spectrum of the MZI-2 with two collapsed regions. (b) The wavelength shift of dip 1 with curvature.

On the other side, simulation models and stress concentrations of MZI-1 and MZI-2 are established and concluded by use of a finite-element-based software, i.e. ANSYS, as shown in Fig. 6. Compared with the collapsed regions, the stress concentrations induced by the peanut-like region and the abrupt taper occur while an identical curvature is applied, this could be noted from the enlarged view in Fig. 6(a). In the meanwhile, there is no stress concentration existed in the two collapsed regions, as shown in Fig. 6(b). However, detailed tests verifying the operational principle will be a topic in our future work.
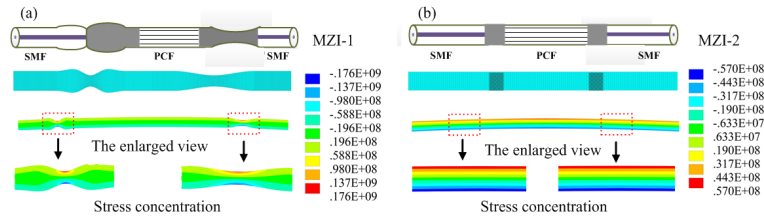
Fig. 6. Numerical simulation of (a) the MZI-1 structure with a peanut-like section and an abrupt taper; (b) the MZI-2 structure with two collapsed regions rather than a peanut-like section and an abrupt taper.

## 3. Conclusion

In summary, we have experimentally demonstrated a compact and highly sensitive MZI for curvature sensing, the length of which is less than 3 mm. And it only requires simple fabrication including splicing. The unique MZI based a PCF exhibits a high curvature sensitivity of 50.5 nm/m$^{-1}$ and a temperature sensitivity of 11.7 pm/°C. The low temperature cross-sensitivity can find lots of application in the field of curvature sensing.